Controls on the magmatic fraction of extension at mid-ocean ridges

Jean-Arthur Olive, Pierre Dublanchet

▶ To cite this version:

Jean-Arthur Olive, Pierre Dublanchet. Controls on the magmatic fraction of extension at mid-ocean ridges. Earth and Planetary Science Letters, 2020, 549, pp.116541. 10.1016/j.epsl.2020.116541 . hal-02921482

HAL Id: hal-02921482
https://hal.science/hal-02921482

Submitted on 25 Aug 2020

HAL is a multi-disciplinary open access archive for the deposit and dissemination of scientific research documents, whether they are published or not. The documents may come from teaching and research institutions in France or abroad, or from public or private research centers.

L'archive ouverte pluridisciplinaire **HAL**, est destinée au dépôt et à la diffusion de documents scientifiques de niveau recherche, publiés ou non, émanant des établissements d'enseignement et de recherche français ou étrangers, des laboratoires publics ou privés.

*Manuscript
Click here to view linked References

Controls on the magmatic fraction of extension at mid-ocean ridges

Jean-Arthur Olive[1*] and Pierre Dublanchet[2]

[1]*Laboratoire de Géologie, Ecole Normale Supérieure / CNRS UMR 8538, PSL Research University, Paris 75005, France.*

[2]*MINES ParisTech, PSL Research University, Centre de Géosciences, Fontainebleau 77305, France.*

**Corresponding author: olive@geologie.ens.fr*

Keywords

Mid-ocean ridge; seafloor spreading; normal faults; diking; submarine volcanism.

Highlights

- Magmatic component of seafloor spreading (*M*) increases non-linearly with spreading rate.
- Stress interactions between fault slip events and magma intrusions provide physical basis for *M*.
- Axial lithosphere thickness and rate of pressure build-up in sills are primary controls on *M*.
- Transitions between modes of seafloor spreading reflect thresholds in axial lithosphere thickness.

Abstract

The fraction M of plate separation accommodated by magma emplacement at mid-ocean ridges has been recognized as the main control on seafloor spreading modes, yet the factors that control M itself are poorly understood. Here we put forward a simple theoretical framework explaining M in terms of short-term cycles of earthquakes and dike intrusions interacting with one another by modulating the stress state of the ridge axis. Axial lithospheric thickness and the rate of pressure build-up in shallow, replenishing magma sills are the two main parameters controlling M in our simulations. Combined with plausible scenarios for the increase of pressure build-up rate and the decrease of lithospheric thickness with increasing spreading rate, our model appropriately brackets available measurements of M from slow, intermediate, and fast-spreading ridges. Our model further suggests that the transitions between major modes of seafloor spreading (detachment faulting, symmetric faulting, and fully-magmatic) correspond to thresholds in axial lithospheric thickness, and that the great variability in M at slow and ultraslow ridges directly reflects along-axis variability in thermal structure. More generally, this implies that the balance between bottom-up magmatic heating and top-down hydrothermal cooling fully determines the time-averaged rate of magmatic intrusions in the brittle lithosphere, and thus the modes of mid-ocean ridge faulting which shape ~2/3 of Earth's surface.

1. Introduction

Seafloor spreading at mid-ocean ridges (MORs) typically involves a combination of tectonic and magmatic processes. Adiabatic decompression melting in the asthenosphere produces magma, which ascends to the ridge axis and crystallizes in sills, dikes or lava flows, forming new oceanic crust. Magmatic emplacement is accompanied by normal faulting, which dissects the brittle upper crust into discrete blocks that undergo uplift and tilting as they are advected off-axis (MacDonald et al., 1996). These processes interact over geological time to shape elongated, regularly spaced abyssal hills: the most common landform on the surface of the Earth (e.g., Kappel and Ryan, 1986).

The long-term (>100 kyr) partitioning of tectonic and magmatic extension at MORs is straightforwardly quantified by summing the heaves of normal faults located within a certain distance to the axis (e.g., Escartín et al., 1999; Schouten et al., 2010). The ratio of magmatically accommodated extension to total plate separation —commonly referred to as M **(Fig. 1a)**— exceeds ~0.9 at fast-spreading ridges (full spreading rate $U \geq 8$ cm/yr) such as the East Pacific Rise (Cowie et al., 1993; Buck et al., 2005; Escartín et al., 2007). At intermediate-spreading MORs ($5 \leq U < 8$ cm/yr), M typically ranges between ~0.7 and ~0.95 (Ito and Behn, 2008), although values in excess of 0.95 have recently been reported locally along the Chile Ridge and the Southeast Indian Ridge (Howell et al., 2016). Variability in the M fraction is maximized at slow ($1.5 \leq U < 5$ cm/yr) and ultraslow ($U <1.5$ cm/yr) MORs. These ridges are characterized by the along-axis juxtaposition of sections with symmetrically faulted (staircase-like) topography, and sections populated by large-offset detachment faults shaping oceanic core complexes and other irregular bathymetric highs (Escartín et al., 2008; Sauter et al., 2011). M ranges between ~0.6 and ~0.8 at symmetrically faulted sections of the Mid-Atlantic ridge (Cowie et al., 1993; Ito and Behn, 2008; Olive and Escartín, 2016). At detachment-bearing sections of the Mid-Atlantic Ridge, M typically varies between ~0.2 and ~0.6 (Behn and Ito, 2008; MacLeod et al., 2009; Schouten et al., 2010). It can reach zero in amagmatic sections of the ultraslow Southwest Indian Ridge, where the seafloor consists of serpentinized peridotite exhumed by detachment faults (Dick et al., 2003; Sauter et al., 2011; Cannat et al., 2019).

Mechanical models suggest that M is the primary control on MOR tectonics (Buck et al., 2005). This includes the average spacing and maximum offset of normal faults, the presence of an axial valley vs. an axial high, and the development of symmetric faults vs. detachments (Behn and Ito, 2008; Ito and Behn, 2008; Tucholke et al., 2008; Olive et al., 2010; 2015; Tian and Choi, 2017; Liu and Buck, 2018; 2020; Howell et al., 2019). The primary effect of the M parameter is to modulate the rate at which an active fault formed in thin axial lithosphere will migrate off-axis, encountering progressively thicker and stronger lithosphere. At some point, breaking a new fault in thin axial lithosphere becomes more energetically favorable than continuing to slip on a fault that has moved off-axis. The greater the M, the sooner this point is reached, meaning that faults form in closer succession on either side of the axis, and accumulate less total slip. This leads to regularly spaced, symmetric abyssal hills. When M is close to 0.5, faults can remain at the ridge axis for extended periods of time and accumulate very large offsets, making detachment faulting possible (Buck et al., 2005). Values of $M < 0.5$ enable faults to migrate towards the axis, which in numerical models results in complex inward- and outward-dipping faults that cross-cut each other (Tucholke et al., 2008; Olive et al., 2010; Bickert et al., 2020).

A common limitation of all the models listed above is that they treat M as an empirical input parameter that cannot be determined from other observables that characterize MOR axes. Measurements show that M increases non-linearly with spreading rate (Olive et al., 2015) in a manner that resembles the increase in magma flux ($\Phi_C = H_C \times U$, with H_C the thickness of the magmatic crust) from ultraslow to fast MOR (e.g., Cannat et al., 2008) **(Fig. 1a)**. Even though the M parameter is often used interchangeably with "magma supply", it has never been quantitatively related to Φ_C, let alone spreading rate. It is also important to note that M only refers to magma intruded in the brittle lithosphere, and ignores melt emplaced in the ductile portion of the ridge axis, which Olive et al. (2010) argued does not impact fault evolution. One might further expect that the strength and thickness of axial lithosphere should affect the modes of shallow melt emplacement, and therefore the *M* value (e.g., Keller et al., 2013).

Here we propose a quantitative framework that identifies first-order controls on M, and explains its non-linear increase with spreading rate **(Fig. 1a)**. Our approach is rooted in the fact that on human time scales, seafloor spreading primarily manifests as normal faulting earthquakes, which can reach magnitudes up to ~6.5 (e.g., Solomon et al., 1988; Cowie et al., 1993; Olive and Escartín, 2016), as well as dike intrusion events that are typically ~1-m wide and sometimes lead to a seafloor eruption (e.g., Qin and Buck, 2008; Tan et al., 2016). We design the simplest possible analytical model of tectono-volcanic cycles, in which plate separation on decadal time scales is either taken up by a dike or an increment of fault slip, depending on the ever-evolving thresholds for magmatic intrusion and fault slip. Averaging the model behavior over many cycles yields an effective *M* value that reflects the influence of spreading rate, lithospheric thickness and melt flux to the ridge axis.

2. A simple model of tectono-magmatic interactions

2.1. Governing equations

We consider an idealized mid-ocean ridge axis (**Fig. 1b**) subjected to a full plate separation rate U, which deforms over a characteristic cross-axis length scale L ~ 10 km. The brittle on-axis lithosphere has a thickness H and overlies a sill-like axial melt lens (AML) located immediately below the brittle-ductile transition. Horizontal stresses at the axis (at depth z below seafloor) consist of a lithostatic component partially relieved by pore pressure, and a horizontal tectonic component $\Delta\sigma_{xx}$ such that

$$\sigma_{xx}(z,t) = -\rho g(1-\lambda)z + \Delta\sigma_{xx}(t), \quad (1)$$

where ρ is the density of the crust (2900 kg/m^3), and g is the acceleration of gravity (9.8 m/s^2). λ denotes fluid pressure normalized by lithostatic pressure $\rho g z$ and will be assumed hydrostatic, i.e., $\lambda = \rho_w/\rho$ = 0.34 (with ρ_w the density of water) except near the roof of the AML where $\lambda = 0$. The horizontal tectonic stress (positive in tension) is assumed to continuously increase over time at a rate prescribed by the far-field plate separation rate:

$$\frac{\partial \Delta\sigma_{xx}}{\partial t} = \frac{EU}{L}, \quad (2)$$

where *E* is the Young's modulus of axial lithosphere. A plausible range for *E* is 5–30 GPa (Heap et al., 2020). In the following we will use *E* = 10 GPa unless otherwise specified, and a Poisson's ratio ν = 0.25. $\Delta\sigma_{xx}$ however cannot increase to infinity and can reach either a tectonic threshold $\Delta\sigma_{xx}^F$, which triggers a seismic (or aseismic) slip event on a fault, or a magmatic threshold $\Delta\sigma_{xx}^M$, which triggers the intrusion of a vertical dike.

The tectonic threshold is determined by assuming the ridge axis is bounded by an optimally-oriented, cohesionless normal fault of friction coefficient μ = 0.6. The static strength of the fault is thus reached when

$$\Delta\sigma_{xx}(t = t_F) = \Delta\sigma_{xx}^F = \frac{\mu\rho g(1-\lambda)H}{\mu+\sqrt{1+\mu^2}}. \quad (3)$$

Equation (3) corresponds to the strength of the fault averaged over the thickness of the brittle lithosphere (e.g., Behn and Ito, 2008). For simplicity, we assume that a tectonic event occurring at time t_F corresponds to an increment in fault slip δ_F in the horizontal direction (e.g., δ_F = 1 m for a magnitude ~6 earthquake with a standard stress drop of ~1 MPa). Such events induce compression at the axis, which instantaneously relieves a small portion of the built-up horizontal tectonic stress. We model this effect by subtracting a stress increment from $\Delta\sigma_{xx}$ after each event:

$$\Delta\sigma_{xx}(t = t_F^+) = \Delta\sigma_{xx}(t = t_F^-) - E\,\frac{\delta_F}{L}. \qquad (4)$$

At certain times, the total horizontal stress at the base of the brittle lithosphere may reach the rocks' tensile strength T_0 (~1 MPa), triggering the intrusion of a dike of width δ_F = 1 m (Kelemen and Aharonov, 1998; Qin and Buck, 2008). This is because magmatic overpressure p_M in the AML (or a sill-like region within the AML) imparts an increase in total horizontal stress near the edges of the area undergoing replenishment and pressurization (Wilcock et al., 2009). This is illustrated in Supplementary Figure S1. The additional tensile stress above the sill is proportional to magmatic overpressure, and may be exacerbated by stress concentrations around sharp edges or irregularities along the top of the AML. The zero-dimensional nature of our approach prevents us from incorporating these effects in a systematic manner. We therefore assume that the increase in horizontal tension near a pressurized sill is equal to magmatic overpressure and thus fluctuates at a rate imposed by the dynamics of magmatic replenishment. The area above the AML is known to be impermeable to fluid circulation (Gillis 2008). It therefore experiences a confining pressure equal to $p_w + \rho g H$, where p_w is water pressure at the seafloor (19.6 MPa for 2000 m depth). With these assumptions, the threshold for diking can be expressed as

$$-p_w - \rho g H + \Delta\sigma_{xx} + p_M = T_0\,, \qquad (5)$$

which can be recast as:

$$\Delta\sigma_{xx}(t = t_M) = \Delta\sigma_{xx}^M(t = t_M) = T_0 - p_M(t = t_M) + p_w + \rho g H\,. \qquad (6)$$

When the threshold described by equation (6) is reached at time t_M, the instantaneous emplacement of a dike imparts an increment of compression on the axis, which we model as:

$$\Delta\sigma_{xx}(t = t_M^+) = \Delta\sigma_{xx}(t = t_M^-) - E\,\frac{\delta_M}{L}. \qquad (7)$$

Equation (6) shows that the diking threshold decreases through time as magma overpressure builds up. We assume that this occurs at a constant rate $\dot{p}_M$, which depends on the volume flux of magma that continuously replenishes the AML. As the intrusion of a dike temporarily connects the AML to the seafloor, it likely lowers magma pressure to a static state, meaning that magmatic overpressure drops to zero following a diking event:

$$p_M(t = t_M^+) = 0. \qquad (8)$$

When this occurs, the magma intrusion threshold is maximized:

$$\Delta\sigma_{xx}^{M,MAX} = T_0 + p_w + \rho g H\ . \qquad (9)$$

Finally, we assume that slip events on ridge-bounding faults, which relax the built-up axial stress $\Delta\sigma_{xx}$, do not otherwise influence the ever-changing threshold for dike initiation $\Delta\sigma_{xx}^M(t)$.

2.2. Choice of parameter values

2.2.1. Axial lithospheric thickness

The thickness of axial lithosphere is a critical parameter in our model. It corresponds to the depth of the brittle-ductile transition, where the shallowest melts can pool, and below which no seismicity occurs. At sections of MORs that are magmatically robust enough for melt to be seismically imaged, the depth to the shallowest AML reflector (circles in **Fig. 2a**) constitutes a good proxy for the base of the brittle lithosphere (Sinton and Detrick, 1992; Phipps-Morgan and Chen, 1993). This dataset is however very scarce at slow MORs. There, the seismogenic depth as measured from OBS-based micro-earthquake surveys (e.g., Grevemeyer et al., 2019) constitutes a reasonable estimate of *H* (squares in **Fig. 2a**). To fully account for the scatter in the data, we empirically bracket our estimates between two end-member trends of lithospheric thickness vs. spreading rate, using the mathematical form:

$$H(U) = H_{MIN} + (H_{MAX} - H_{MIN})e^{-\frac{U}{\Delta U}}. \qquad (10)$$

The "thinnest" and "thickest" trends (red and blue curves in **Fig. 2a**) correspond to H_{MIN}, H_{MAX}, and ΔU of 1.2 km, 6 km, 1.8 cm/yr; and 2 km, 26 km, and 2.7 cm/yr, respectively.

2.2.2. Magmatic pressure rate

The rate at which magma pressure increases with time in a continuously replenishing reservoir is by far the most difficult parameter to constrain in our model. Indirect estimates can be obtained by measuring and modeling seafloor inflation that sometimes precedes eruptions. To date, this has only been achieved at Axial seamount, a volcano located on a hot-spot influenced section of the Juan de Fuca ridge (Nooner and Chadwick, 2016), and at 9º50' N on the East Pacific Rise (Nooner et al., 2014). We focus on the latter example, which —being more representative of a typical fast MOR segment— can be extrapolated to construct a trend of $\dot{p}_M$ with spreading rate (**Fig. 2b**). Nooner et al. (2014) deployed pressure sensors along an axis-perpendicular profile to measure seafloor uplift over several years. Sensors located near the axial trough uplifted at ~7 cm/yr while sensors located ~10 km off-axis did not exhibit resolvable vertical motion. Upon fitting this deflection profile with two end-member models of magma pocket inflation (See Supplementary Material), we obtain ranges of plausible pressure rates: between 1.9×10^{-1} and 1.9×10^{3} Pa/s for a Mogi model, and between 4.0×10^{-5} and 2.3×10^{-3} Pa/s for a laccolith model (**Fig. 2b**)

The large discrepancy between these estimates highlights the difficulty of quantifying magma pressure build-up through direct observation. We therefore complement this approach with an order-of-magnitude assessment of $\dot{p}_M$ vs. spreading rate largely following the model of Aharonov and Kelemen (1998). We treat a magmatic sill as a horizontal, elliptical pressurized crack of width *w*, and infinite along-axis extent. The maximum thickness *h* of the sill is linked to magma overpressure (Rubin, 1995a) according to:

$$h = 2(1-\nu)(1+\nu)\frac{\Delta P}{E}w\ . \qquad (11)$$

From equation (11) we can relate the pressure rate to the flux of magma inflating the sill (Φ, volume flux into a single sill, per unit length along axis):

$$\Phi = \pi(1-\nu)(1+\nu)\frac{\dot{p}_M}{2E}w^2\ . \qquad (12)$$

The total magma flux leading to a mean crustal thickness H_C (= 6 km) is simply $\Phi_C = H_C U$. Assuming this flux gets equally partitioned within *N* magma sills, we can derive an order-of-magnitude estimate for pressure rate as a linear function of spreading rate:

$$\dot{p}_M = \frac{2E}{\pi(1+\nu)(1-\nu)}\frac{H_C U}{N w^2}\ . \qquad (13)$$

A high estimate of $\dot{p}_M$ vs. *U* can be obtained using a high estimate of *E* (30 GPa, Heap et al., 2020) and low estimates for *w* (50 m) and *N* (10) (Aharonov and Kelemen, 1998). Conversely, *E* = 5 GPa, *w* = 500 m (Wilcock et al., 2009), and *N* = 100 provide a low estimate of $\dot{p}_M$. A geometric average of these two end-members yields a reasonable intermediate estimate of $\partial\dot{p}_M/\partial U$ = 6.312 $\times 10^7$ Pa.m^{-1}. The full range of estimates is plotted in **Fig. 2b**, and is consistent with inferences of $\dot{p}_M$ based on seafloor deflection.

3. Results

The co-evolution of $\Delta\sigma_{xx}$ and p_M over time is solved numerically through a forward Euler discretization of equation (2), with instantaneous stress changes prescribed when tectonic or magmatic thresholds are reached (equations 4, 7 and 8). The corresponding codes are provided as part of the Supplementary Material. Typical model behavior is illustrated in **Fig. 3**, which represents 4 characteristic types of MOR section. **Fig. 3a** corresponds to a slow-spreading segment with an 8-km thick axial lithosphere. It shows the continuous decrease of the diking threshold from its peak (post-eruption) value of ~250 MPa, in response to increasing magma pressure. For a new eruption to become possible, the diking threshold has to fall below the faulting threshold (~63 MPa). Assuming a value of $\dot{p}_M$ appropriate for this spreading rate (5×10^{-2} Pa/s at U = 2.5 cm/yr according to our intermediate estimate, **Fig. 2b**), this occurs within ~130 years, which sets the characteristic recurrence time of magmatic intrusions. About 2 earthquakes typically occur in 130 years, because far-field extension increases the axial stress fast enough to overcome the characteristic earthquake stress drop twice in this time frame. Two out of three "events" of seafloor spreading are thus tectonic. When averaged over time scales of kyrs to tens of kyrs, this translates to an M value of 0.3. In **Fig. 3b**, the spreading and pressure rates are the same, but on-axis lithospheric thickness is lowered to 3 km. This lowers both the diking and faulting thresholds, as well as the difference between them. The recurrence time of eruptions is thus reduced to ~50 years, which sometimes allows for an earthquake to occur, and sometimes does not. The time-averaged M is consequently increased to 0.7. Similar mechanisms are at play in **Fig. 3c**, which corresponds to a faster spreading rate, thinner lithosphere, and greater pressure build-up rate. Finally, in **Fig. 3d**, the pressure rate is so fast that earthquakes cannot occur within the short eruption recurrence time (~7 yrs). This leads to fully-magmatic seafloor spreading (M = 1).

To further explore the primary controls on M, we carried out 80000 simulations spanning a wide range of pressure rates and spreading rates, with lithospheric thickness indexed on spreading rate following the "thinnest" and "thickest" end-members introduced in **Fig. 2a**. Contour lines in **Fig. 4** shows the time-averaged *M* values yielded by each of these simulations. In **Fig. 2c**, we show the trends of *M* vs. spreading rate obtained upon combining the intermediate scenario for $\dot{p}_M$ vs. spreading rate (solid curve in **Fig. 2b**, red lines in **Fig. 4**) with the two end-member scenarios for lithospheric thickness vs. spreading rate (red and blue curves in **Fig. 2a**). These two trends successfully bracket our dataset of *M* vs. spreading rate.

4. Discussion

4.1. Primary controls on *M*

The results shown in **Fig. 2** suggest that the non-linear increase in *M* with spreading rate may reflect both the (possibly linear) increase in the rate of magma pressure build-up (**Fig. 4**), and the change in lithospheric thickness, which is most pronounced at slow rates. The key effect of increasing lithospheric thickness is to increase the difference between the peak magmatic threshold stress $\Delta\sigma_{xx}^{M,MAX}$ and the tectonic threshold $\Delta\sigma_{xx}^{F}$ (**Fig. 3**). This in turn increases the characteristic recurrence time of magmatic intrusions, which can be approximated as:

$$\tau_M = \frac{\Delta\sigma_{xx}^{M,MAX} - \Delta\sigma_{xx}^{F}}{\dot{p}_M}. \quad (14)$$

This approximation is valid as long as an earthquake stress drop remains small compared to the difference between peak magmatic and tectonic thresholds. This ensures that an eruption closely follows the moment when $\Delta\sigma_{xx}^{M}$ becomes smaller than $\Delta\sigma_{xx}^{F}$. Once the timing of intrusions is known, an expression for *M* straightforwardly follows:

$$M = min\left(\frac{\delta_M}{U\tau_M}, 1\right). \quad (15)$$

The predictions from this analytical approximation closely match the values of M estimated from our numerical simulations over a wide range of pressure and spreading rates (**Fig. 4**).

By combining the above equations with our linear model for $\dot{p}_M$ vs. U (equation 13), we can cancel out spreading rate from the expression of M (valid for $M < 1$), and obtain:

$$M = \frac{\delta_M \frac{\partial \dot{p}_M}{\partial U}}{P_0 + \rho g \gamma H}, \qquad (16)$$

where γ is a dimensionless factor introduced for concision: $\gamma = 1 - \mu'(1 - \lambda)$, with $\mu' = \frac{\mu}{\mu + \sqrt{1+\mu^2}}$. P_0 denotes a characteristic pressure: $P_0 = T_0 + p_w$, which is typically small (~10 MPa) compared to the $\rho g \gamma H$ term (~100 MPa). Equation (16) is plotted in **Fig. 5a** for several values of $\partial \dot{p}_M / \partial U$, which represent different scenarios for the increase in magma volume flux (expressed as pressure increase in a shallow sill) with spreading rate. This graph clearly shows that a key influence of spreading rate on M actually occurs through changes in lithospheric thickness H. In fact, of all the parameters controlling M in our model, lithospheric thickness is the one that changes most significantly from slow to fast spreading rates (**Fig. 2a**). The fact that using end-member estimates of H vs. U appropriately brackets the available dataset of M vs. U (**Fig. 2c**) further supports the idea that variability in lithospheric thickness is a strong source of variability in M at MORs.

Bracketing the M dataset in **Fig. 2c** works best when using our intermediate estimate for $\partial \dot{p}_M / \partial U$ (6.312×10^7 Pa.m^{-1}), which corresponds to the geometric average of high and low estimates that span several orders of magnitude (Section 2.2.2, **Figs. 2b, 5b**). The value of $\partial \dot{p}_M / \partial U$ depends on parameters such as crustal thickness and the number (N) and characteristic cross-axis extent (w) of inflating sills (equation 13). These parameters are likely to vary significantly from one ridge section to another, but may not show a systematic trend with respect to spreading rate. Crustal thickness is for example known to remain roughly constant at ~6 km for most MORs, except along ultraslow ridges where it can oscillate between ~0 and ~10 km from segment to segment, because of extreme along-axis melt focusing (e.g., Dick et al., 2003; Cannat et al., 2008; Sauter et al., 2011; Niu et al., 2015) (See Section 4.2). Unlike crustal thickness, the cross-axis extent of shallow magma reservoirs is not well characterized. Seismically-imaged AMLs generally appear narrower at faster ridges (e.g., Lowell et al., 2020), but magma pressure may only build up in a small portion of the AML prior to an eruption (Wilcock et al., 2009; Nooner and Chadwick, 2016), making w (of order 10^2 – 10^3 m) difficult to constrain. Finally, intrusion width δ_M is also a strong control on M in equation (16). Qin and Buck (2008) pointed out that the typical width of dikes observed at ophiolites and MORs is ~1 m, and does not clearly correlate with spreading rate. These authors however noted that greater tectonic stresses and a strong magmatic input could theoretically enable intrusions as wide as a few meters.

4.2. Implications for seafloor spreading regimes

4.2.1. Symmetric vs. detachment faulting at slow spreading rates

Our model provides a straightforward explanation for the increased variability in M at slower spreading rates (**Fig. 2c**) by directly attributing it to the increased variability in axial lithospheric thickness (**Fig. 2a**). This variability is largely due to focusing of melt towards segment centers, which makes the lithosphere warmer and thinner there compared to segment ends (Cannat, 1996). Variability in magma supply also occurs on a larger scale at slow and ultraslow MORs, and shapes 50–100-km long MOR sections with axial volcanic ridges, symmetrically faulted abyssal hill morphology (M ~ 0.6–0.8), and shallow seismicity. These sections alternate with areas characterized by a more complex, "asymmetric" morphology associated with widespread detachment faulting (M ~ 0.2–0.6), deeper and more active seismicity, deeper melt fractionation, a greater occurrence of active hydrothermal sites, and in some extreme cases at ultraslow spreading ridges: a much thinner or virtually absent igneous crust (Dick et al., 2003; Escartín et al., 2008; Tucholke et al., 2008; Sauter et al., 2011; Olive and Escartín, 2016; Cannat et al., 2019).

In our theoretical framework, M values of ~0.5 and below, which enable detachment faulting (Buck et al., 2005), are a direct consequence of the lithosphere being locally thicker than a threshold value of ~5 km (**Fig. 5a**; **Fig. 6**) for a given magmatic influx. This is fully consistent with the fact that microseismicity appears confined within 5–6 km below seafloor at abyssal hill-bearing sections of the Northern Mid-Atlantic Ridge, while detachment-bearing sections produce micro-earthquakes down to ~12 km (e.g., Barclay et al., 2001; Parnell-Turner et al., 2017). Detachment bearing sections may therefore receive an influx of melt comparable to symmetrically-faulted sections, but allow a lesser fraction of this melt to intrude their colder, thicker brittle lithosphere. The exact value of the threshold thickness for detachment faulting however strongly depends on $\partial \dot{p}_M/\partial U$ (dashed green curve in **Fig. 5b**), which itself depends on crustal thickness and a number of other poorly-constrained parameters. This could explain why symmetrically faulted sections of ultraslow MORs such as Segment 27 of the Southwest Indian Ridge can host micro-earthquakes ~10 km below seafloor (Yu et al., 2018). This segment is indeed characterized by ~10-km thick crust (Niu et al., 2015), a likely result of extreme along-axis magma focusing (Dick et al., 2003). Such a high volume flux of magma could plausibly cause anomalously high pressure build-up rates in magma reservoirs (compared to the global trend of $\dot{p}_M$ vs. spreading rate shown in **Fig. 2b**), which would enable M values in excess of 0.5 even in 10-km thick lithosphere (**Fig. 5**).

If for a given volume flux of magma, the time-averaged M is mainly set by lithospheric thickness, it is important to keep in mind that lithospheric thickness itself is strongly controlled by magmatic input. In a broad sense, the thermal structure of a MOR reflects a balance between heat advected upwards from the asthenosphere —through magma ascent and mantle flow— and heat transferred through the lithosphere by hydrothermal circulation (e.g., Chen and Morgan, 1990; Phipps-Morgan and Chen, 1993). Models that balance magmatic input and hydrothermal output are generally successful at explaining the thermal state of MORs receiving a steady magma supply, as they accurately replicate the depth to the shallowest AML at intermediate to fast rates (**Fig. 2a**) (e.g., Phipps-Morgan and Chen, 1993). In these models, the heat input stems from magmatic emplacement below the lithosphere (e.g., Maclennan et al., 2004), yet repeated dike intrusions in the brittle domain are also likely to influence the equilibrium thermal structure (e.g., Behn and Ito, 2008). Feedbacks are also likely to exist between hydrothermal and tectonic processes. For example, fracturing associated with the damage zones of large-offset faults could increase crustal permeability, and thus the vigor of hydrothermal convection in detachment-bearing ridge sections (Escartín et al., 2008). Enhanced cooling would further thicken the lithosphere, which in turn would promote lower M values that favor detachment faulting, in a self-reinforcing feedback loop that would stabilize the detachment forming regime.

4.2.2. Transition to fully-magmatic spreading at faster spreading rates

Another important feature of our model is that it predicts conditions under which seafloor spreading becomes fully magmatic (M = 1). This specifically occurs when axial lithosphere becomes thinner than a critical thickness that is straightforwardly obtained by setting M = 1 in equation (16), and strongly depends on $\partial \dot{p}_M/\partial U$ (**Fig. 5**). In the framework of Buck et al. (2005) and Liu and Buck (2018; 2020), reaching M = 1 marks the transition between a mode of spreading dominated by tectonic stretching, where M directly controls the characteristics of faults that bound an axial valley (Behn and Ito, 2008; Olive et al., 2015), and a buoyancy-dominated regime where an axial high forms due to the upward load exerted on the lithosphere by low-density melts (**Fig. 6**). In this regime, only small inward- and outward-dipping faults form to accommodate near-axis lithospheric flexure (e.g., Escartín et al., 2007). In real systems, the transition from axial valley to axial rise occurs at intermediate rates, between 5.5 and 7.5 cm/yr (Dick et al., 2003), which corresponds to axial lithospheric thicknesses between ~2 and ~5 km (**Fig. 2a**). This is well accounted for by our model when using values $\partial \dot{p}_M/\partial U$ close to 10^8 Pa.m^{-1} (**Fig. 5b**), which are well within the plausible range estimated in Section 2.2.2 and plotted in **Fig. 2b**. This said, the extent to which the transition from axial valley to axial high truly represents a transition to fully-magmatic spreading remains debatable. Ito and Behn (2008) for example showed that alternating between periods of M = 0 and M = 1 lasting kyrs to tens of kyrs could allow the growth of an axial high with a time-averaged M < 1, as is seen at some intermediate and fast-spreading MORs. In numerical models, this requires the axis to be weak enough to rapidly develop positive relief during intermittent, fully-magmatic phases.

A major transition in seafloor spreading modes was also observed in recent analog experiments conducted by Sibrant et al. (2018) using Ludox. This viscous colloidal dispersion behaves as an elastic-brittle material when mixed with salt. By pouring a saline solution from the top down into a tank filled with Ludox, Sibrant et al. (2018) were able to model a brittle lithosphere that diffusively thickens off-axis and overlies a fluid asthenosphere. Upon subjecting this system to increasing extension rates, they observed a transition from fault-accommodated plate separation to a regime dominated by vertical Ludox "intrusions". They proposed that this occurs when the axial thickness of the lithosphere (controlled by extension rate) falls below the characteristic size of the process zone of mode-I cracks. They further showed that this reasoning could be upscaled to real MORs to predict the switch to fully-magmatic extension at fast-spreading rates. An interesting analogy can be drawn with our approach, in which intrusion-dominated spreading occurs when (1) magma pressure builds up at a rapid rate in shallow reservoirs and (2) axial lithosphere is thin enough that the difference between peak magmatic and tectonic thresholds is low. Both of these conditions should be met at fast-spreading MORs. In the experiments of Sibrant et al. (2018), it is unclear whether fluid pressure builds up at the base of the lithosphere prior to intrusion events, and whether the rate of pressure increase is affected by spreading rate. It may instead be controlled solely by the buoyancy difference between pure and saline Ludox. If the pressure build-up rate is sufficiently fast, Ludox intrusions may become so frequent that the differential stress required for faulting is never reached at the axis. In any case, our respective modeling approaches agree that the transition to fully magmatic spreading involves a threshold of axial lithospheric thickness (**Fig. 5b**; **Fig. 6**).

4.3. Model limitations and possible improvements

We have attempted to construct the simplest possible model that explains global trends of *M* vs. spreading rate in terms of stress interactions between magmatic and tectonic events. By doing so, we have made a number of simplifying assumptions that we briefly discuss here. First, we model the seismic cycle as a time-predictable process (e.g., Shimazaki and Nakata, 1980) with a constant stress build-up rate, triggering stress, and earthquake stress drop, all of which are likely to fluctuate through time in a real system. In particular, we have only considered magnitude ~6 earthquakes, each accounting for 1 m of horizontal slip with total slip and 1 MPa of stress drop. In reality, normal faulting earthquakes at MORs follow a Gutenberg-Richter distribution with relatively high b-values (Olive and Escartín, 2016), which means that most of the seismically-accommodated extension is accounted for by the largest earthquakes. The significant deficit of MOR earthquakes compared to their expected moment release however suggests that a sizable portion of tectonic extension may occur aseismically, particularly at faster-spreading ridges (Cowie et al., 1993; Frohlich and Wetzel, 2007; Olive and Escartín, 2016). This idea is backed up by recent numerical models of MOR seismic cycles (Mark et al., 2018).

Second, we rely on a simplified model for intrusion triggering which involves reaching the tensile strength of the lithosphere at the roof of a magma pocket under the combined influence of magmatic overpressure and tectonic stress. This is consistent with recent seismological investigations of the early stage of an East Pacific Rise eruption, which began with synchronous ruptures distributed over a distance spanning multiple distinct magma reservoirs (Tan et al., 2016). This was interpreted as multiple, independently replenished AMLs —potentially out-of-sync with respect to magma pressure— being brought to failure synchronously by tectonic loading. Our model obviously does not capture the complexity of such events, warranting further investigations of the 3-D stress field around replenishing sills (e.g., Wilcock et al., 2009; Supplementary Fig. S1), and the consideration of alternative triggering criteria for example based on fracture mechanics (e.g., Sibrant et al., 2018). Another limitation of our model is its simplified treatment of magmatic pressure build-up, which we assume to occur at a constant, poorly constrained rate, lumping together a number of complex processes related to sill emplacement and replenishment in the lower oceanic crust. On the one hand, whether sill replenishment happens continuously or in pulses depends on the way magma ascends to the base of the lithosphere and through the axial mush zone, which could involve wave-like transport (Parnell-Turner et al., 2020). On the other hand, the link between sill inflation rate and pressure build-up potentially involves damping of pressure changes by viscous relaxation of hot rocks above the magma (e.g., Kelemen and Aharonov, 1998) and poro-elastic effects in the surrounding mush zone. Better characterizing the stress changes imparted by replenishing magma reservoirs at MOR axes before and after intrusions will be key to improving our theory. This will involve continuous monitoring of MOR axes through seafloor geodesy and seismology (e.g., Nooner and Chadwick, 2016), with the caveat that extrapolating short-term measurements to geological time scales will remain difficult until we at least capture a full seismic / volcanic cycle, particularly at a slow ridge section not influenced by a hot spot (Tolstoy et al., 2001; Dziak et al., 2004). Another difficulty in bridging time scales of seafloor spreading is the increasing amount of evidence for temporal fluctuations in MOR activity on periods ranging from 10s of kyrs to millions of years (e.g., Parnell-Turner et al., 2020). This has led Tolstoy (2015) to question whether the behavior of MORs that we observe today is representative of past or longer-term activity.

The last important limitation of our approach is the assumption that dikes and faults compete to release the elastic strain energy stored in axial lithosphere, but have no possibility of triggering each other. Such interactions have however been observed several times at rifts and ridges. Calais et al. (2008) for example documented a 2007 slow slip event on a normal fault that likely promoted the intrusion of a dike in the eastern branch of the East African Rift. Tolstoy et al. (2001) reported the reciprocal phenomenon of a migrating dike triggering a dozen magnitude ~5 earthquakes along the normal faults that bound the axial valley of the Gakkel ridge (85ºN), throughout most of the year 1999. This raises the question of whether tectonic extension at MORs primarily occurs during or in response to magmatic events. We note that the 20+ km length of the valley-bounding faults at Gakkel makes them susceptible to nucleating magnitude ~6–6.5 earthquakes (Wells and Coppersmith, 1994). Such events could occur separately from intrusions and would account for ~3 times more slip over the same along-axis distance compared to ~10 magnitude-5 earthquakes. Again, a longer record of observations is needed to assess whether the tectonic extension that accompanies diking is systematically small compared to the associated magmatic extension, and/or to purely tectonic spreading events. Dziak et al (2004) for example estimated that all the seismicity associated with the 2001 dike intrusion event at the Lucky Strike segment of the Mid-Atlantic Ridge amounted to centimeters of horizontal extension, which would be negligible if the dike alone accommodated ~1 m of extension. In any case, available observations warrant the development of more detailed seismic cycle models of MOR faults (e.g., Mark et al., 2018) that interact with an inflating sill and episodic dike intrusions. This will require detailed constraints on the geometry of the fault(s) relative to that of the magmatic plumbing system, as static stress transfers often display sharp spatial variations (Supplementary Figure S1). The modes of volcano-tectonic or tectono-volcanic triggering may thus be strongly dependent on the local geometry of the ridge, e.g., a deeper magmatic system at a slower MOR would influence faults within a broader horizontal area compared to a shallow sill-dike system at a fast MOR (e.g., Tolstoy et al., 2001).

5. Conclusions

We have designed a simple theoretical framework explaining the long-term partitioning of magmatic and tectonic extension at MORs in terms of short-term cycles of earthquakes and dike intrusions that interact with one another by modulating the stress state of the ridge axis (**Figs. 1, 3**). Axial lithospheric thickness and the rate of pressure build-up in shallow, replenishing magma sills are the two main parameters controlling *M* in our model (**Fig. 4**). We constructed plausible scenarios for the increase of pressure rate with spreading rate, as well as end-member trends for lithospheric thickness across MOR spreading rates (**Fig. 2a, b**). This allowed us to bracket the observed non-linear increase in *M* and relate its reduced variability with increasing spreading rate (**Fig. 2c**) to reduced along-axis variability in lithosphere thickness.

To first-order, spreading rate controls the flux of magma that reaches the ridge axis. The thermal component of this flux fuels hydrothermal circulation, which modulates the strength and thickness of axial lithosphere. The mass component of this flux contributes to setting the pace of pressure build-up in shallow sills, which together with lithosphere thickness, sets the value of *M*. This in turn controls the intensity of tectonic deformation, which could affect the vigor of hydrothermal circulation through pervasive fracturing of the crust, exerting a feedback on lithosphere thickness. The dichotomy between symmetrically faulted and detachment-bearing sections of slow MORs could thus reflect thresholds in lithosphere thickness under a near constant along-axis magma flux (**Figs. 5 & 6**). Extreme focusing of melt along the axis of ultraslow MORs however points to the combined action of a spatially-varying magma flux and lithosphere thickness in shaping symmetrically-faulted segments and quasi-amagmatic sections. On the other end of the spectrum, the large, spatially uniform influx of magma to fast MORs ensures a uniformly thin lithosphere with frequent intrusions, which makes fully magmatic spreading possible. Overall, modes of seafloor spreading reflect a balance between magmatic, tectonic, and hydrothermal processes, raising the question of whether temporal fluctuations in magma supply can alter the stability of these equilibria and trigger regime transitions.

Acknowledgements

We wish to thank our editor Jean-Philippe Avouac as well as Maya Tolstoy and an anonymous reviewer for their helpful feedback. This work greatly benefited from discussions with Mark Behn, Roger Buck, Mathilde Cannat, Javier Escartín and Garrett Ito. J.-A.O. was supported by an Emergence(s) - Ville de Paris grant, and NSF grant OCE-1654745. This work relied exclusively on previously published data. All the codes necessary to reproduce our results are provided as part of the Supplementary Material, and are available at https://github.com/jaolive/TectoMagMOR.

Appendix A.

Supplementary Material related to this article consists of:

• Supplementary Information (.pdf file). Additional details regarding the modeling of seafloor inflation at the East Pacific Rise to infer pressure increase rates in a shallow magma reservoir. Instructions on how to use the supplementary codes. This file includes 4 Supplementary Figures.

• Supplementary Code: M_across_rates.m; a MATLAB script producing Figs. 1a, 2, 3, 4 and 5.

• Supplementary Code: tectono_magmatic_fcn.m; MATLAB implementation of the toy model of tectono-volcanic cycles.

• Supplementary Text files: .txt files for use by the MATLAB scripts, containing datasets of M (M_data.txt), micro-earthquake depths (depth_of_microEQs.txt), and AML depths (depth_of_AMLs.txt).

References

Barclay, A.H., Toomey, D.R., Solomon, S.C., 2001. Microearthquake characteristics and crustal V_P/V_S structure at the Mid-Atlantic Ridge, 35ºN, Journal of Geophysical Research, 106, 2017-2034.

Behn, M.D., Ito, G., 2008. Magmatic and tectonic extension at mid-ocean ridges: 1. Controls on fault characteristics. Geochemistry, Geophysics, Geosystems, 9. doi:10.1029/2008GC001965.

Bickert, M., Lavier, L., Cannat, M., 2020. How do detachment faults form at ultraslow mid-ocean ridges in a thick axial lithosphere? Earth and Planetary Science Letters, 533. doi:10.1016/j.epsl.2019.116048.

Buck, W.R., Carbotte, S., Mutter, C.Z., 1997. Controls on extrusion at mid-ocean ridges, Geology, 25, 935-938.

Buck, W.R., Lavier, L., Poliakov, A.N.B., 2005. Modes of faulting at mid-ocean ridges. Nature, 434, 719–723. doi: 10.1038/nature03358.

Calais, E., d'Oreye, N., Albaric, J., Deschamps, A., Delvaux, D., Déverchère, J., Ebinger, C., Ferdinand, R.W., Kervyn, F., Macheyeki, A.S., Oyen, A., Perrot, J., Saria, E., Smets, B., Stamps, D.S., Wauthier, C., 2008. Strain accommodation by slow slip and dyking in a youthful continental rift, East Africa. Nature, 456. doi:10.1038/nature07478.

Cannat, M., 1996. How thick is the magmatic crust at slow spreading oceanic ridges? Journal of Geophysical Research, 101(B2), 2847-2857.

Cannat, M., Sauter, D., Bezos, A., Meyzen, C., Humler, E., Le Rigoleur, M., 2008. Spreading rate, spreading obliquity, and melt supply at the ultraslow spreading Southwest Indian Ridge. Geochemistry, Geophysics, Geosystems, 9(4). doi:10.1029/2007GC001676.

Cannat, M., Sauter, D., Lavier, L., Bickert, M., Momoh, E., Leroy, S., 2019. On spreading modes and magma supply at slow and ultraslow mid-ocean ridges. Earth and Planetary Science Letters, 519, 223-233. doi:10.1016/j.epsl.2019.05.012.

Chen, Y., Morgan, W.J., 1990. A nonlinear rheology model for mid-ocean ridge axis topography. Journal of Geophysical Research, 95(B11), doi:10.1029/JB095iB11p17583.

Cowie, P.A., Scholz, C.H., Edwards, M., Malinverno, A, 1993. Fault strain and seismic coupling on mid-ocean ridges. Journal of Geophysical Research, 98(B10), 17,911-17,920.

Dick, H.J.B., Lin, J., Schouten, H., 2003. An ultraslow-spreading class of ocean ridge. Nature, 426.

Dziak, R.P., Smith, D.K., Bohnenstiehl, D.R., Fox, C.J., Desbruyeres, D., Matsumoto, H., Tolstoy, M., Fornari, D.J., 2004. Evidence of a recent magma dike intrusion at the slow spreading Lucky Strike segment, Mid-Atlantic Ridge. Journal of Geophysical Research, 109, doi:10.1029/2004JB003141.

Escartín, J., Cowie, P.A., Searle, R.C., Allerton, S., Mitchell, N.C., MacLeod, C.J., Slootweg, A.P., 1999. Quantifying tectonic strain and magmatic accretion at a slow spreading ridge segment, Mid-Atlantic Ridge, 29°N. Journal of Geophysical Research, 104, 10421-10437. https://doi.org/10.1029/1998JB900097.

Escartín, J., Soule, S.A., Fornari, D.J., Tivey, M., Schouten, H., Perfit, M, 2007. Interplay between faults and lava flows in construction of the upper oceanic crust: The East Pacific Rise crest 9°25'-58'N. Geochemistry, Geophysics, Geosystems, 8 (Q06005).

Escartín, J., Smith, D.K., Cann, J.R., Schouten, H., Langmuir, C.H., Escrig, S., 2008. Central role of detachment faults in accretion of slow-spreading oceanic lithosphere. Nature, 455, 7214, 790–794. doi: 10.1038/nature07333.

Frohlich, C., Wetzel, L.R., 2007. Comparison of seismic moment release rates along different types of plate boundaries, Geophysical Journal International, 171, 909-920.

Gillis, K.M., 2008. The roof of an axial magma chamber: a hornfelsic heat exchanger, Geology, 36, 299–302.

Grevemeyer, I., Hayman, N.W., Lange, D., Peirce, C., Papenberg, C., Van Avendonk, H.J.A., Schmid, F., Gómez de La Peña, L., Dannowski, A., 2019. Constraining the maximum depth of brittle deformation at slow- and ultraslow-spreading ridges using microseismicity. Geology, 47(11), 1069-1073. doi:10.1130/G46577.1.

Heap, M.J., Villeneuve, M., Albino, F., Farquharson, J.I., Brothelande, E., Amelung, F., Got, J.-L., Baud, P., 2020. Towards more realistic values of elastic moduli for volcano modelling. J. Volc. Geotherm. Res., 390. doi:10.1016/j.jvolgeores.2019.106684.

Howell, S., Ito, G., Behn, M.D., Martinez, F., Olive, J.-A., Escartín, J., 2016. Magmatic and tectonic extension at the Chile Ridge: Evidence for mantle controls on ridge segmentation. Geochemistry, Geophysics, Geosystems, 17. doi:10.1002/2016GC006380.

Howell, S., Olive, J.-A., Ito, G., Behn, M.D., Escartín, J., Kaus, B., 2019. Seafloor expression of oceanic detachment faulting reflects gradients in mid-ocean ridge magma supply. Earth and Planetary Science Letters, 516.

Ito, G., Behn, M.D., 2008. Magmatic and tectonic extension at mid-ocean ridges: 2. Origin of axial morphology. Geochemistry, Geophysics, Geosystems, 9(Q08O10).

Kappel, E.S., Ryan, W.B.F., 1986. Volcanic episodicity and a non-steady rift valley along Northeast Pacific spreading centers: Evidence from Sea MARC I. Journal of Geophysical Research, 91(B14), 13925-13940.

Kelemen, P., Aharonov, E., 1998. Periodic formation of magma fractures and generation of layered gabbros in the lower crust beneath oceanic spreading ridges, in Faulting and Magmatism at Mid-Ocean Ridge, Geophysical Monograph Series, 106, Buck, W.R. et al. (editors), AGU, Washington, D.C. doi:10.1029/GM106p0291.

Keller, T., May, D.A., Kaus, B.J.P., 2013. Numerical modelling of magma dynamics coupled to tectonic deformation of lithosphere and crust. Geophysical Journal International, 195(3), 1406-1442.

Liu, Z., Buck, W.R., 2018. Magmatic controls on axial relief and faulting at mid-ocean ridges. Earth and Planetary Science Letters, 491. doi:10.1016/j.epsl.2018.03.045.

Liu, Z., Buck, W.R., 2020. Global trends of axial relief and faulting at plate spreading centers imply discrete magmatic events. Journal of Geophysical Research, doi:10.1029/2020JB019465.

Lowell, R.P., Zhang, L., Maqueda, M.A.M., Banyte, D., Tong, V.C.H., Johnston, R.E.R., Harris, R.N., Hobbs, R.W., Peirce, C., Robinson, A.H., Kolandaivelu, K., 2020. Magma-hydrothermal interactions at the Costa Rica Rift from data collected in 1994 and 2015. Earth and Planetary Science Letters, 531.

Macdonald, K.C., Fox, P.J., Alexander, R.T., Pockalny, R., Gente, P., 1996. Volcanic growth faults and the origin of Pacific abyssal hills. Nature, 380, 125-129.

Maclennan, J., Hulme, T., Singh, S.C., 2004. Thermal models of oceanic crustal accretion: Linking geophysical, geological, and petrological observations. Geochemistry, Geophysics, Geosystems, 5(2).

MacLeod, C.J., Searle, R.C., Murton, B.J., Casey, J.F., Mallows, C., Unsworth, S.C., Achenbach, K.L., Harris, M., 2009. Life cycle of oceanic core complexes. Earth and Planetary Science

Letters, 287, 333-344.

Mark, H.F., Behn, M.D., Olive, J.-A., Liu, Y., 2018. Controls on mid-ocean ridge normal fault seismicity across spreading rates from rate-and-state friction models. Journal of Geophysical Research, 123.

Niu, X., Ruan, A., Li, J., Minshull, T.A., Sauter, D., Wu, Z., Qiu, X., Zhao, M., Chen, Y.J., Singh, S., 2015. Along-axis variation in crustal thickness at the ultraslow spreading Southwest Indian Ridge (50ºE) from a wide-angle seismic experiment. Geochemistry, Geophysics, Geosystems, 16, 468-485, doi:10.1002/2014GC005645.

Nooner, S.L., Webb, S.C., Buck, W.R., Cormier, M.-H., 2014. Post eruption inflation of the East Pacific Rise at 9º50'N. Geochemistry, Geophysics, Geosystems, 15, 2676-2688. doi:10.1002/2014GC005389.

Nooner, S.L., Chadwick, W.W., 2016. Inflation-predictable behavior and co-eruption deformation at Axial Seamount. Science, 354(6318), 1399-1403. doi:10.1126/science.aah4666.

Olive, J.-A., Behn, M.D., Tucholke, B.E., 2010. The structure of oceanic core complexes controlled by the depth-distribution of magma emplacement. Nature Geoscience, 3., 491–495, doi:10.1038/ngeo888.

Olive, J.-A., Behn, M.D., Ito, G., Buck, W.R., Escartín, J., Howell, S., 2015. Sensitivity of seafloor bathymetry to climate-driven fluctuations in mid-ocean ridge magma supply. Science, 350(6258).

Olive, J.-A., Escartín, J., 2016. Dependence of seismic coupling on normal fault style along the Northern Mid-Atlantic Ridge. Geochemistry, Geophysics, Geosystems, 17.

Parnell-Turner, R., Sohn, R.A., Peirce, C., Reston, T.J., MacLeod, C.J., Searle, R.C., Simão, N.M., 2017. Oceanic detachment faults generate compression in extension. Geology, 45(10), 923-926. doi:10.1130/G39232.1.

Parnell-Turner, R., Sim, S.J., Olive, J.A., 2020. Time-dependent crustal accretion on the Southeast Indian Ridge revealed by Malaysia Airlines MH370 search, Geophysical Research Letters, doi:10.1029/2020GL087349.

Phipps Morgan, J., Chen, Y.J., 1993. The genesis of oceanic crust: Magma injection, hydrothermal circulation, and crustal flow. Journal of Geophysical Research, 98(B4), 6283-6297. doi:10.1029/92JB02650.

Qin, R., Buck, W.R., 2008. Why meter-wide dikes at spreading centers? Earth and Planetary Science Letters, 265, 466-474.

Rubin, A.M., 1995a. Propagation of magma-filled cracks. Annual Review of Earth and Planetary Sciences, 23, 287-336.

Sauter, D., Cannat, M., Rouméjon, S., Andréani, M., Birot, D., Bronner, A., Brunelli, D., Carlut, J., Delacour, A., Guyader, V., Macleod, C.J., Manatschal, G., Mendel, V., Ménez, B., Pasini, V., Ruellan, E., Searle, R.C., 2013. Continuous exhumation of mantle-derived rocks at the Southwest Indian Ridge for 11 million years. Nature Geoscience, 6, 314–320.

Schouten, H., Smith, D.K., Cann, J.R., Escartín, J., 2010. Tectonic versus magmatic extension in the presence of core complexes at slow-spreading ridges from a visualization of faulted seafloor topography. Geology, 38(7), 615–618. doi: 10.1130/G30803.1.

Shimazaki, K., Nakata, T., 1980. Time-predictable recurrence model for large earthquakes. Geophysical Research Letters, 7(4), 279-282.

Sibrant, A.L.R., Mittelstaedt, E., Davaille, A., Pauchard, L., Aubertin, A., Auffray, L., Pidoux, R., 2018. Accretion mode of oceanic ridges governed by axial mechanical strength. Nature Geoscience, 11, 274-279. doi:10.1038/s41561-018-0084-x.

Singh, S.C., Crawford, W.C., Carton, H., Seher, T., Combier, V., Cannat, M., Canales, J.P., Düsünür, D., Escartín, J., Miranda, J.M., 2006. Discovery of a magma chamber and faults beneath a Mid-Atlantic Ridge hydrothermal field. Nature, 442. doi:10.1038/nature05105.

Sinton, J.M., and Detrick, R.S., 1992. Mid-ocean ridge magma chambers. Journal of Geophysical Research, 97, 197-216. doi:10.1029/91JB02508.

Solomon, S.C., Huang, P.Y., Meinke, L., 1988. The seismic moment budget of slowly spreading ridges. Nature, 334, 58–60.

Tan, Y.J., Tolstoy, M., Waldhauser, F., Wilcock, W.S.D., 2016. Dynamics of a seafloor spreading episode at the East Pacific Rise. Nature, 540, 261-265.

Tian, X., Choi, E., 2017. Effects of axially variable diking rates on faulting at slow spreading mid-ocean ridges. Earth and Planetary Science Letters, 458, 14–21.

Tolstoy, M., Bohnenstiehl, D.R., Edwards, M.H., Kurras, G.J., 2001. Seismic character of volcanic activity at the ultraslow-spreading Gakkel ridge. Geology, 29, 1139–1142.

Tolstoy, M., 2015. Mid-ocean ridge eruptions as a climate valve. Geophysical Research Letters, 42, 1346–1351.

Tucholke, B.E., Behn, M.D., Buck, W.R., Lin, J., 2008. Role of melt supply in oceanic detachment faulting and formation of megamullions. Geology, 36, 455-458.

Wells, D.L., Coppersmith, K.J., 1994. New empirical relationships among magnitude, rupture length, rupture width, rupture area and surface displacement. Bulletin of the Seismological Society of America, 84, 974–1002.

Wilcock, W.S.D., Hooft, E.E., Toomey, D.R., McGill, P.R., Barclay, A.H., Stakes, D.S., Ramirez, T.J., 2009. The role of magma injection in localizing black-smoker activity. Nature Geoscience, 2, 509-513.

Yu, Z., Li, J., Niu, X., Rawlinson, N., Ruan, A., Wang, W., Hu, H., Wei, X., Zhang, J., Liang, Y., 2018. Lithospheric structure and tectonic processes constrained by microearthquake activity at the central ultraslow-spreading Southwest Indian Ridge (49.2° to 50.8°E). Journal of Geophysical Research, 123, 6247-6262.

Figure 1 – **a.** Fraction of magmatic extension across spreading rates. MAR: Mid-Atlantic Ridge; GSC: Galapagos Spreading Center; JdF: Juan de Fuca Ridge; CR: Chile Ridge; SEIR: Southeast Indian Ridge; ELSC: Eastern Lau Spreading Center; EPR: East Pacific Rise. Data from Cowie et al. (1993); Ito and Behn (2008); Olive and Escartín (2016) and Howell et al. (2016). **b.** Model setup.

Figure 2 – **a.** Estimates of axial lithospheric thickness from seismically imaged AML depths (circles, as compiled by Buck et al., 1997; Singh et al., 2006) and depth of micro-earthquakes (squares, as compiled by Grevemeyer et al., 2019). Colored lines correspond to thick and thin end-members as defined by equation (10). Light-green stars correspond to example cases shown in Fig. 3. Sd: Slow, detachment faulting regime; Ss: Slow, symmetric faulting regime; I: Intermediate; F: Fast. **b.** Modeled pressure rate vs. spreading rate (equation 13), with intermediate estimate as continuous line and high and low estimates as dashed lines. Estimates from seafloor deflection at the EPR (See Supplementary Material) are shown as vertical bars (Mo: Mogi; La: Laccolith models). **c.** Same dataset of M vs. U as in Fig. 1, with curves corresponding to the thin (red) and thick (blue) end-members models.

Figure 3 – Modeled tectono-volcanic cycles (axial stress $\Delta\sigma_{xx}$, in black, and diking threshold $\Delta\sigma_{xx}^{M}$, in red, vs. time) in 4 example configurations. **a.** slow, detachment-bearing ridge section (Sd in Fig. 2): H = 8 km; U = 2.5 cm/yr. **b.** slow, symmetrically faulted ridge section (Ss): H = 3 km; U = 2.5 cm/yr. **c.** Intermediate-spreading MOR (I): H = 2.5 km; U = 6 cm/yr. **d.** Fast-spreading MOR (F): H = 1.5 km; U = 15 cm/yr. In each example the pressure rate is 3.1560×10^{7} $Pa.m^{-1}.s^{-2}$ times the spreading rate (intermediate estimate) from Fig. 2b.

Figure 4 – Model predictions of M as a function of spreading rate and magma pressure rate. The color code corresponds to the analytical approximation from equations (14) and (15) while black contour lines (spanning M = 0.1 to 1, with increments of 0.1) show results from the simulations. The red line is the average estimate of pressure rate vs. U, and the dashed red line is the high estimate. Panels a and b respectively correspond to the thin and thick lithosphere end-members of H vs. U shown in Fig. 2a.

Figure 5 – **a.** Lithospheric thickness control on M for different values of $\partial \dot{p}_M / \partial U$ corresponding to the vertical bars in panel b. The solid curves correspond to the low (blue), intermediate (black) and high (red) estimates of pressure rate vs. spreading rate from Fig. 2b. **b.** Green dashed curve: critical lithospheric thickness above which extension becomes detachment-dominated (M = 0.5, dashed green circle in panel a), plotted against $\partial \dot{p}_M / \partial U$. Green solid curve: critical lithospheric thickness below which extension becomes fully magmatic (M = 1, solid green circle in panel a). These critical thicknesses are obtained by setting M = 0.5 or 1 in equation (16).

Figure 6 – Schematic diagram of major seafloor spreading modes as a function of spreading rate and axial lithosphere thickness. Vertical orange arrow represents volume flux of magma to shallowest reservoir (orange ellipse), which is assumed to scale linearly with spreading rate. Horizontal dashed lines represent lithosphere thickness thresholds identified in Fig. 5. Each spreading mode corresponds to a case shown in Fig. 3: Sd: Slow, detachment faulting regime; Ss: Slow, symmetric faulting regime; I: Intermediate; F: Fast.

Figure 1

Click here to download Figure: Figure_1_data_model.pdf

a.

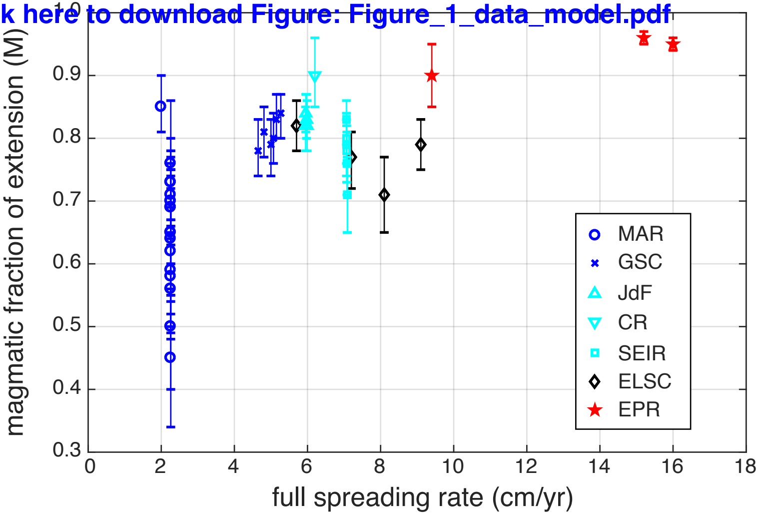

b.

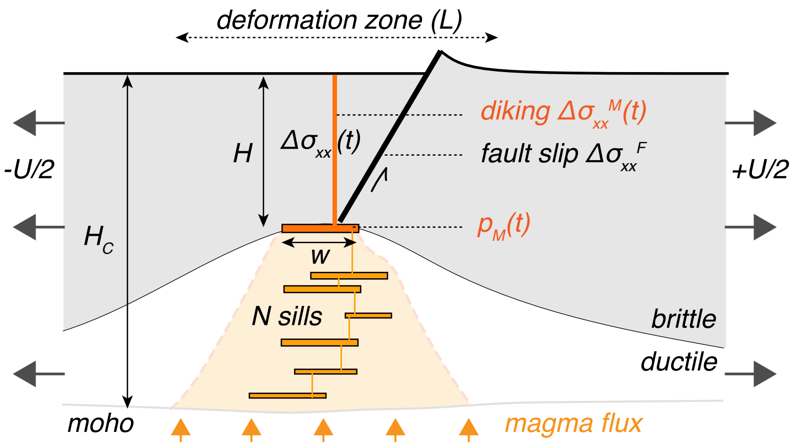

Figure 2

[Click here to download Figure: Figure_2_M_](#)

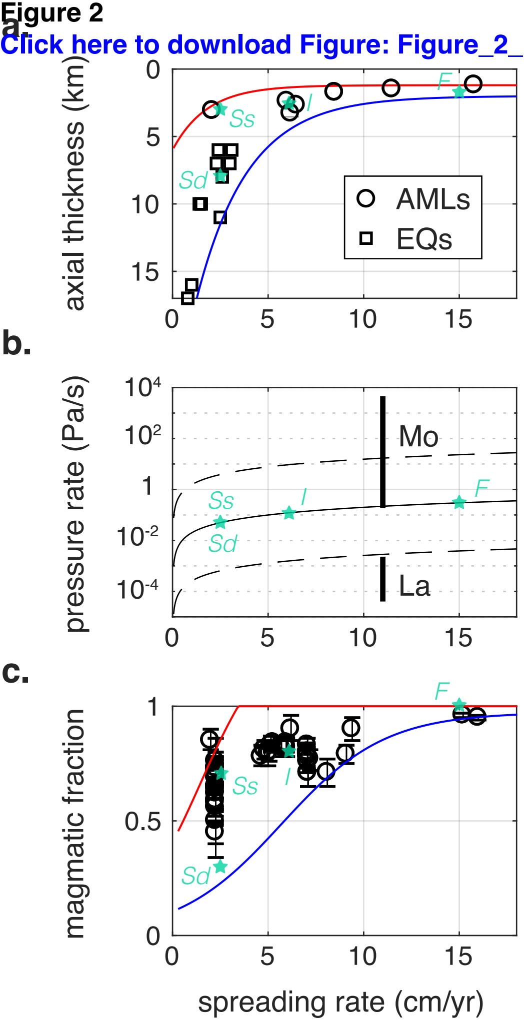

Figure 3

Click here to download Figure: Figure_3_cycles.pdf

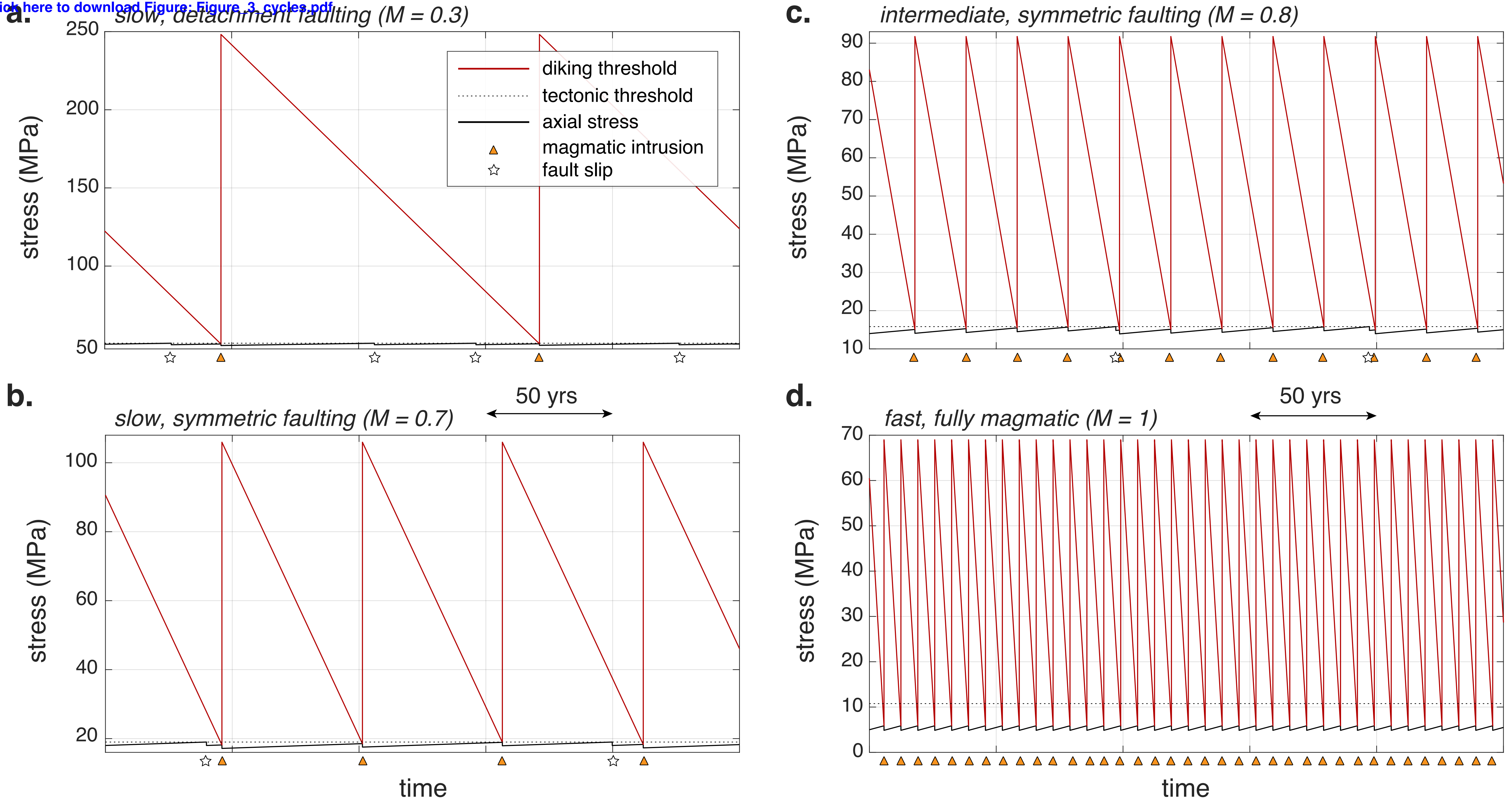

Figure 4

Click here to download Figure: Figure_4_M_maps.pdf

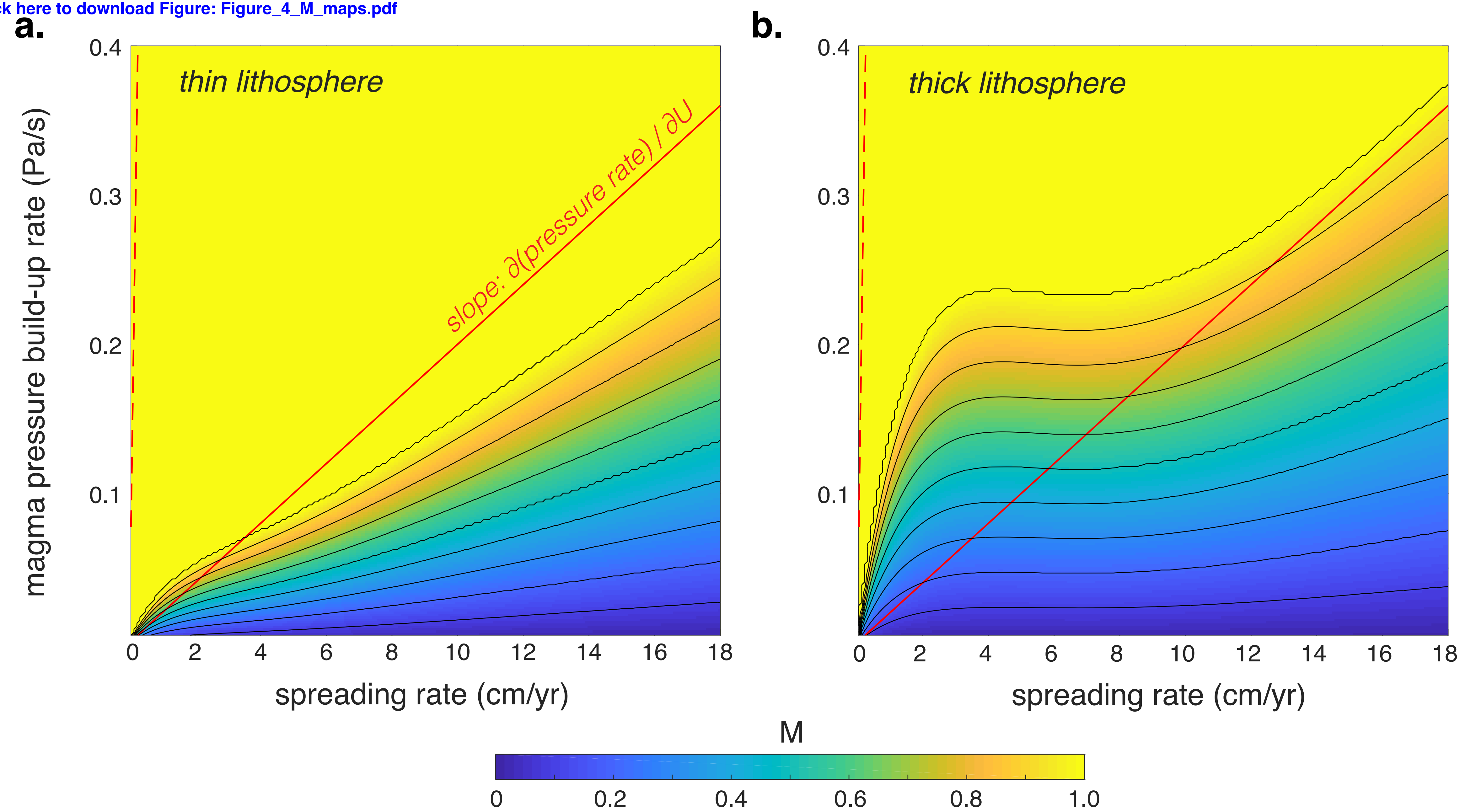

Figure 5
Click here to download Figure: Figure_5_thickness_control.pdf

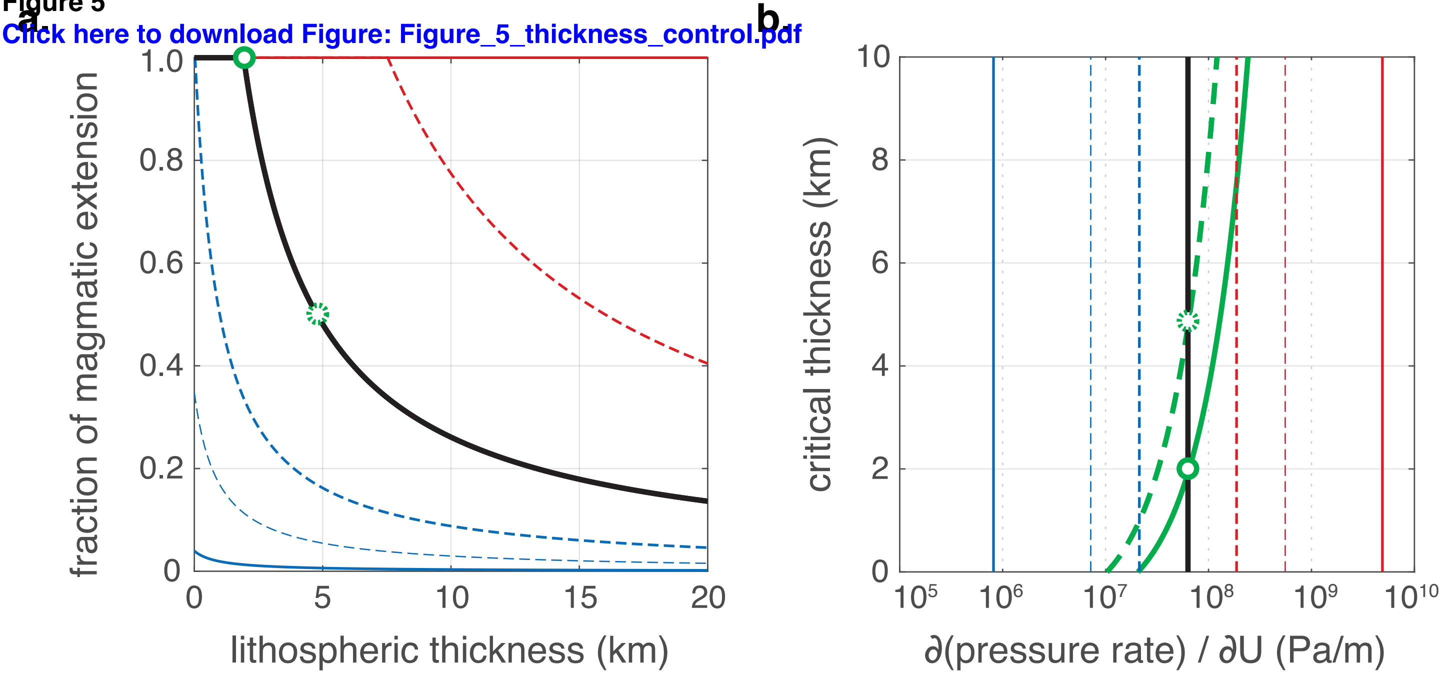

Figure 6
Click here to download Figure: Figure_6_summary_cartoon.pdf

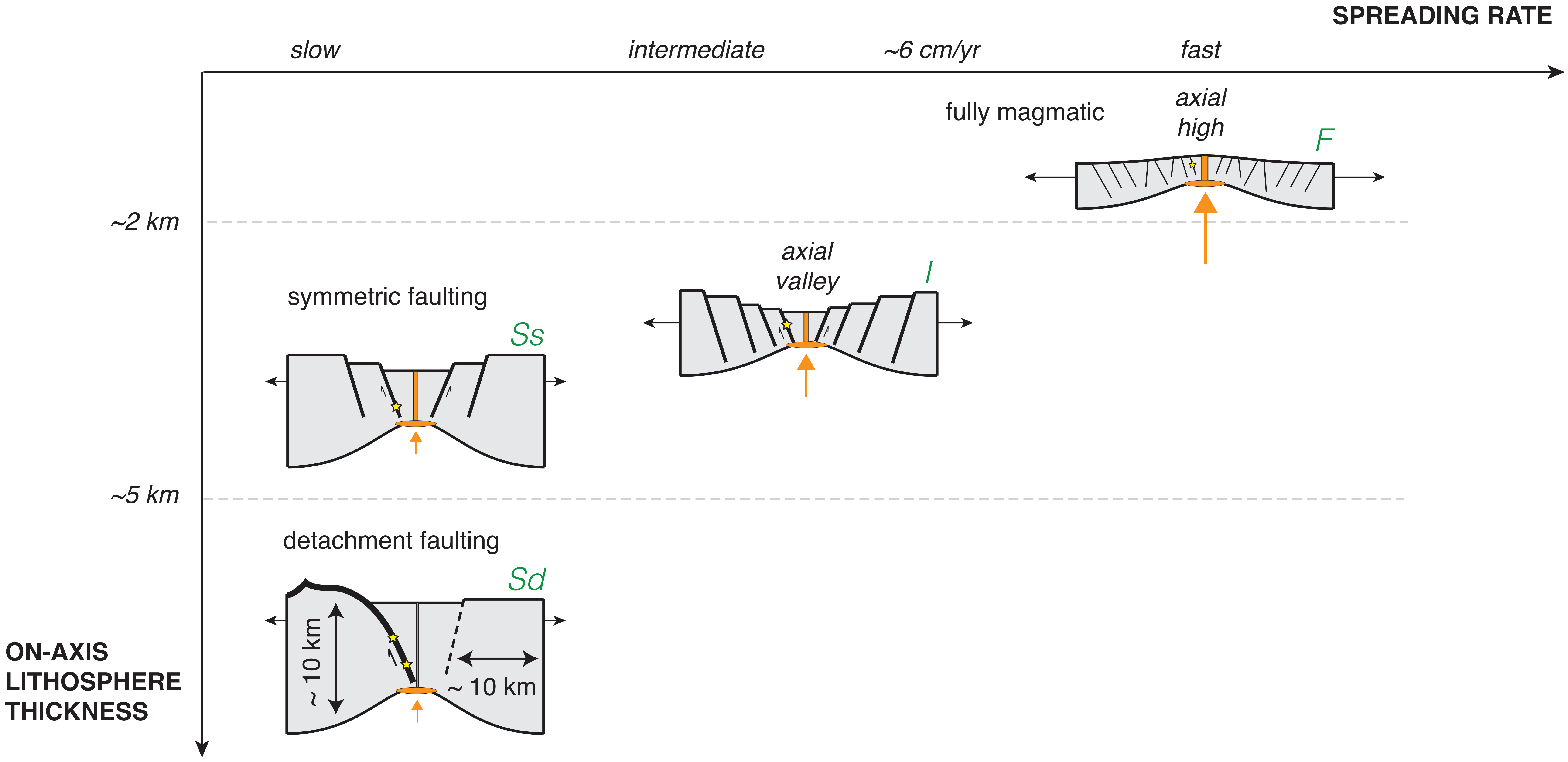

Supplementary Information for "Controls on the magmatic fraction of extension at mid-ocean ridges"

Jean-Arthur Olive [1]and Pierre Dublanchet [2]

[1]Laboratoire de Géologie, École Normales Supérieure / CNRS UMR 8538, PSL Research University, Paris 75005, France

[2]MINES ParisTech, PSL Research University, Centre de Géosciences, 35 rue saint-honoré 77305 Fontainebleau, France

Contents of this file

Text S1: Magmatic pressure rates at the East Pacific Rise

Here we provide two different estimates of the magmatic pressure rate characterizing the inflation of a shallow melt lens at the axis of a mid-ocean ridge. We specifically rely on the seafloor uplift rates recorded by Nooner, Webb, Buck, and Cormier (2014), and fit the measurements with two end-member models of magma reservoir.

Corresponding author: J.-A. Olive, Laboratoire de Géologie, École Normale Supérieure / CNRS UMR 8538, PSL Research University, Paris 75005, France (olive@geologie.ens.fr)

The first one is a Mogi point source within an elastic half-space (Mogi, 1958). In this case, the surface vertical displacement rates v are given by:

$$v(r) = \frac{(1-\nu)V_0}{\pi} \frac{d}{(r^2+d^2)^{3/2}}, \tag{1}$$

where d is the depth of the source, r is the radial distance from the source at the seafloor, ν is the Poisson's ratio of the elastic half-space and V_0 an equivalent volumetric flux, defined as:

$$V_0 = \frac{\pi \dot{p}_m a^3}{G}, \tag{2}$$

$\dot{p}_m$, a and G being the magmatic pressure rate, the source radius and the shear modulus of the elastic medium respectively. Here, the Poisson's ratio ν is considered constant $\nu = 0.25$ and we invert for the depth d and the volumetric flux V_0 using a grid search algorithm. Confidence intervals on d and V_0 are presented in figure S2a., and the comparison between acceptable models and the data are shown in figure S2b. V_0 ranges from 1.2×10^6 to 4.8×10^6 m^3.yr^{-1} at the 60% confidence level (figure S2a.). End-member values for the source radius ($a = 50$ m and $a = 500$ m) and the shear modulus ($G = 2$ GPa and $G = 12$ GPa, Heap et al. (2020)) lead to plausible pressure rates $\dot{p}_m$ ranging from 1.9×10^{-1} to 4.6×10^3 Pa.s^{-1}.

We then inverted the same dataset using the laccolith model of (Turcotte & Schubert, 2002). In this setup, the lithosphere is treated as a thin elastic plate of rigidity D uplifted above a magma reservoir (of full width L and overpressure p_m). The surface vertical displacement are given by:

$$v(r) = \begin{cases} \frac{\dot{p}_m}{24D}\left(r^4 - \frac{L^2r^2}{2} + \frac{L^4}{16}\right) & \text{if } r \leq L/2 \\ 0 & \text{if } r > L/2 \end{cases} \tag{3}$$

D is given by:

$$D = \frac{EH^3}{1-\nu^2}, \tag{4}$$

where E, ν and H are the Young's modulus, the Poisson's ratio and the thickness of the elastic plate. The Poisson's ratio and the thickness are considered fixed here at $\nu = 0.25$ and $H = 1.5$ km (Fig. 2a, see main text). We invert for the magmatic pressure rate $\dot{p}_m$ and the laccolith width L assuming two extreme scenarios for the Young's modulus ($E = 5$ GPa and $E = 30$ GPa, corresponding to $G = 2$ GPa and $G = 12$ GPa, Heap et al. (2020)). Results are shown in figures S3 ($E = 5$ GPa) and S4 ($E = 30$ GPa). To the 60% confidence level, $\dot{p}_m$ ranges from 4.0×10^{-5} to 2.3×10^{-3} Pa.s^{-1}.

Text S2: Reproducing results and figures with supplementary codes

We provide supplementary codes to fully reproduce the results and figures from the main text. MATLAB script *M_across_rates.m* plots the analytical model, and uses function *tectono_magmatic_fcn.m* to run toy model simulations. To generate Figs. 1b; 2; 3; 4 and 5, one can run *M_across_rates.m* by setting variable *regime* (line 9) to 'thin' or 'thick' to select an end-member scenario for lithospheric thickness vs. spreading rate (red and blue curves in Fig. 2a). All scripts must be run from the same folder, which must include the three .txt files containing the M (*M_data.txt*), micro-earthquake depth (*depth_of_microEQs.txt*), and AML depth (*depth_of_AMLs.txt*) datasets, respectively.

References

Heap, M. J., Villeneuve, M., Albino, F., Farquharson, J. I., Brothelande, E., Amelung, F., ... Baud, P. (2020). Towards more realistic values of elastic moduli for volcano modelling. *Journal of Volcanology and Geothermal Research*, *390*, 106684.

Mogi, K. (1958). Relations between the eruptions of various volcanoes and the deformations of the ground surfaces around them. *Earthq Res Inst*, *36*, 99–134.

Nooner, S. L., Webb, S. C., Buck, W. R., & Cormier, M.-H. (2014). Post eruption inflation of the east pacific rise at 9 50 n. *Geochemistry, Geophysics, Geosystems*, *15*(6), 2676–2688.

Pollard, D. D., & Segall, P. (1987). Theoretical displacements and stresses near fractures in rock: with applications to faults, joints, veins, dikes, and solution surfaces. In B. K. Atkinson (Ed.), *Fracture mechanics of rock* (p. 277 - 349). London: Academic Press.

Turcotte, D. L., & Schubert, G. (2002). *Geodynamics*. Cambridge university press.

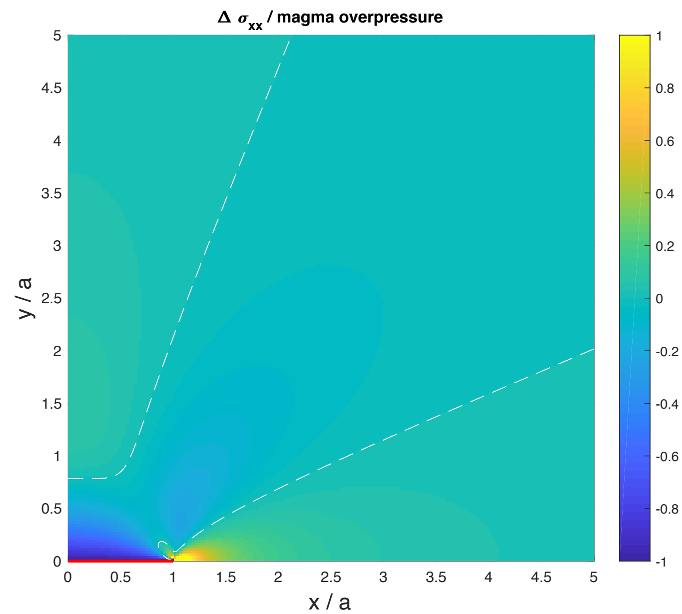

Figure S1. Change in total horizontal stress induced by an over-pressured sill of half-width a (red line), normalized by overpressure (Pollard & Segall, 1987). Yellow lobes show areas where tensile stress builds up and a dike is likely to initiate. Tensile stress perturbation in this region is of same order of magnitude as magmatic overpressure. White dashed lines show contours of zero stress perturbation.

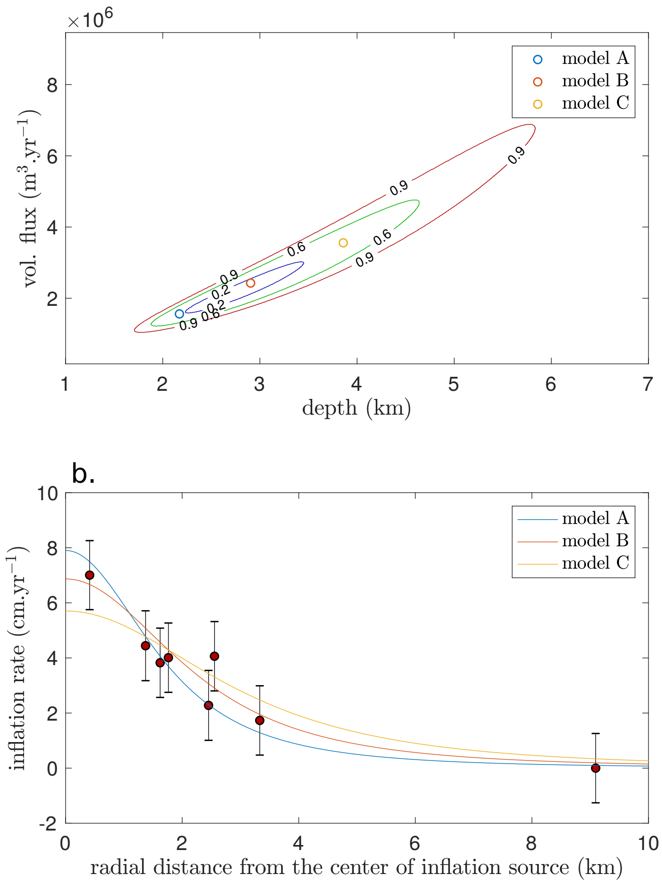

Figure S2. a. Source depths and volumetric fluxes explaining seafloor vertical displacements at the East Pacific Rise following the model of Mogi (1958). Labels on the contours indicate the confidence level. Colored dots indicate the parameters used for the model predictions shown in b. b. Data (red dots) vs. model predictions (colored lines) of equation (1).

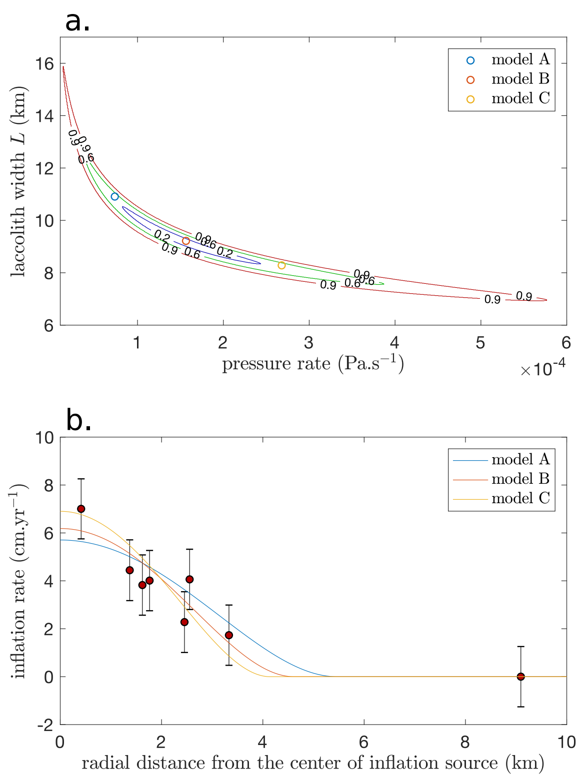

Figure S3. Same figure as figure S2 for the laccolith model of equation (3), assuming $G = 2$ GPa.

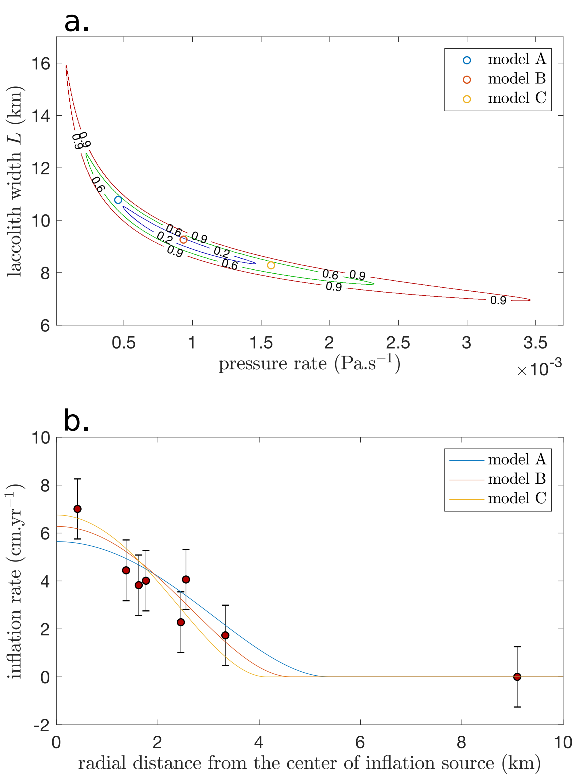

Figure S4. Same figure as figure S2 for the laccolith model of equation (3), assuming $G = 12$ GPa.